

ICAM1 depletion reduces spinal metastasis formation in vivo and improves neurological outcome

Thomas Broggin · Marcus Czabanka · Andras Piffko · Christoph Harms · Christian Hoffmann · Ralf Mrowka · Frank Wenke · Urban Deutsch · Carsten Grötzinger · Peter Vajkoczy

Received: 24 October 2014 / Revised: 9 February 2015 / Accepted: 11 February 2015 / Published online: 25 February 2015
© Springer-Verlag Berlin Heidelberg 2015

Abstract

Introduction Clinical treatment of spinal metastasis is gaining in complexity while the underlying biology remains unknown. Insufficient biological understanding is due to a lack of suitable experimental animal models. Intercellular adhesion molecule-1 (ICAM1) has been implicated in metastasis formation. Its role in spinal metastasis remains unclear. It was the aim to generate a reliable spinal metastasis model in mice and to investigate metastasis formation under ICAM1 depletion.

Material and methods B16 melanoma cells were infected with a lentivirus containing firefly luciferase (B16-luc). Stable cell clones (B16-luc) were injected retrogradely into the distal aortic arch. Spinal metastasis formation was monitored using in vivo bioluminescence imaging/MRI. Neurological deficits were monitored daily. In vivo selected, metastasized tumor cells were isolated (mB16-luc) and

reinjecting intraarterially. mB16-luc cells were injected intraarterially in ICAM1 KO mice. Metastasis distribution was analyzed using organ-specific fluorescence analysis.

Results Intraarterial injection of B16-luc and metastatic mB16-luc reliably induced spinal metastasis formation with neurological deficits (B16-luc:26.5, mB16-luc:21 days, $p < 0.05$). In vivo selection increased the metastatic aggressiveness and led to a bone specific homing phenotype. Thus, mB16-luc cells demonstrated higher number (B16-luc: 1.2 ± 0.447 , mB16-luc: 3.2 ± 1.643) and increased total metastasis volume (B16-luc: $2.87 \pm 2.453 \text{ mm}^3$, mB16-luc: $11.19 \pm 3.898 \text{ mm}^3$, $p < 0.05$) in the spine. ICAM1 depletion leads to a significantly reduced number of spinal metastasis (mB16-luc: 1.2 ± 0.84) with improved neurological outcome (29 days). General metastatic burden was significantly reduced under ICAM1 depletion (control: $3.47 \times 10^7 \pm 1.66 \times 10^7$; ICAM-1^{-/-}: $5.20 \times 10^4 \pm 4.44 \times 10^4$, $p < 0.05$ vs. control)

Conclusion Applying a reliable animal model for spinal metastasis, ICAM1 depletion reduces spinal metastasis formation due to an organ-unspecific reduction of metastasis development.

T. Broggin and M. Czabanka contributed equally to this work.

T. Broggin · M. Czabanka (✉) · A. Piffko · P. Vajkoczy
Department of Neurosurgery, Universitätsmedizin Charite,
Augustenburger Platz 1, 13353 Berlin, Germany
e-mail: marcus.czabanka@charite.de

C. Harms · C. Hoffmann
Department of Experimental Neurology, Universitätsmedizin
Charite, Berlin, Germany

R. Mrowka · F. Wenke
Experimental Nephrology, Universitätsklinikum, Jena, Germany

U. Deutsch
Theodor Kocher Institute, University of Berne, Berne, Germany

C. Grötzinger
Department for Hepatology and Gastroenterology, Charite,
Berlin, Germany

Keywords Experimental spinal metastasis · ICAM-1 · B16 · Spinal compression

Introduction

Improved diagnostics and oncological therapies are causing an increased incidence of spinal metastasis. Currently, 70 % of all oncological patients develop spinal metastasis and 10 % of these patients experience neurological deficits due to epidural myelom compression [1–3]. Therefore, an increasing number of complex surgical therapies have to be

performed to control clinical symptoms [4]. However, the underlying biological mechanisms that govern metastasis formation to the spine remain unknown and therefore, there are no targeted therapies available for these patients. Tumor cell–endothelial cell interactions have been postulated as key mediators of spinal metastasis development [5]. In bone micrometastases, positive expression of the intercellular adhesion molecule-1 (ICAM1) has been described indicating that ICAM1 may influence bone metastasis by regulating tumor cell–endothelial cell interactions during tumor cell dissemination [6]. Based on different experimental and clinical studies, ICAM1 may represent a potential therapeutical target to reduce metastasis formation in different cancers [7–9]. However, the role of ICAM1 in development of spinal metastasis remains unknown. ICAM1 may influence spinal metastasis formation either by altering tumor cell–endothelial cell interactions and thereby changing tumor cell extravasation to the spinal bone. Another potential mechanism may occur after tumor cells have extravasated into spinal bone when interactions between metastatic tumor cells and bone specific microenvironment regulate osteoclast activity and metabolism. It was the aim of this study to characterize an experimental spinal metastasis model in mice, which can be monitored with highly spatial (MRI) and temporal resolution (bioluminescence) to investigate the influence of ICAM1 on spinal metastasis formation *in vivo*.

Materials and methods

Lentiviral vector cloning

To generate a tri-functional reporter vector a multiple cloning backbone (MCS adaptor *T2A*, size 257 bp) harboring two *T2A* self-cleavage sites was used (Fig. 1a). This MCS adaptor was coned in the pcDNA5/FRT vector (Invitrogen). The puromycin gene, the luciferase gene and the *eGFP* were amplified with PCR primers containing appropriate restriction overhangs. Digested PCR products were sequentially cloned in the MCS adaptor yielding a *luciferase-T2A-EGFP-T2A-puromycin* sequence with an open reading frame over the whole reporter sequence. Functionality of the reporter was checked by luciferase reaction, fluorescence imaging and resistance to puromycin in HEK293 cells. Successful and complete *T2A* cleavage was checked by Western-Blot (Data not shown).

Cell line cultivation

B16-F1 (ATCC Nr: CRL-6323), HEK293TN (BioCat, Heidelberg, Germany) and B16-luc infected with FFLUC-GFP-Puro vector construct were routinely maintained at

37 °C with 5 % CO₂ in DMEM (Invitrogen, Carlsbad, CA, USA) supplemented with 10 % FCS, 50 units/ml penicillin and 50 µg/ml streptomycin. B16-luc medium was supplemented 5 µg/ml puromycin.

Lentivirus construction and production

Third-generation lentiviral particles were generated as described previously [10] with the following modification: pFUGW lentiviral transfer plasmids (addgene plasmid 14883, kindly provided by Dr. David Baltimore) were used as a lentiviral transfer vector backbone and *EGFP* was excised by BamHI and XhoI [11]. A 3137 bp insert fragment was isolated from pcDNA5-FR-FF-EGFP coding for *luciferase-T2A-EGFP-T2A-puromycin* cassette. In a second step, the woodchuck hepatitis element *WPRE* was added to the plasmid via Bsu361 and XhoI from a modified version of addgene plasmid 27232 [10, 12]. All constructs were fully sequenced prior to lentiviral particle production. Lentiviral transfer plasmids were co-transfected with packaging plasmids psPAX2 (addgene plasmid 12260) and pMD2.G (addgene plasmid: 12259, both provided by Dr. Didier Trono) into 293TN cells using XtremeGene HP (Roche, Grenzach-Wyhlen, Germany) in OptiMEM (Gibco, Life Technologies, Karlsruhe, Germany). Two harvests of supernatant containing viral particles from the 293TN culture medium were collected 48 and 72 h after transduction. The supernatant was centrifuged at 1790g for 15 min and filtered through a 0.45 µm low protein-binding PVDF membrane (Millipore, Schwalbach, Germany). The viral particles were precipitated using PEGiT according to the manufacturer's instructions (BioCat, Heidelberg, Germany), resuspended and aliquoted in PBS and stored at –80 °C for later use. Viral transduction efficiency was determined from serial dilutions in primary neuronal cultures using EGFP fluorescence as a reporter 48 h after transduction. Viral particles were applied at a multiplicity of infection of approximately 20 with transduction units of 109 per ml after concentration of lentiviral particles. Stable transfected B16-luc cells were selected using puromycin.

Bioluminescence analysis of transfected tumor cells

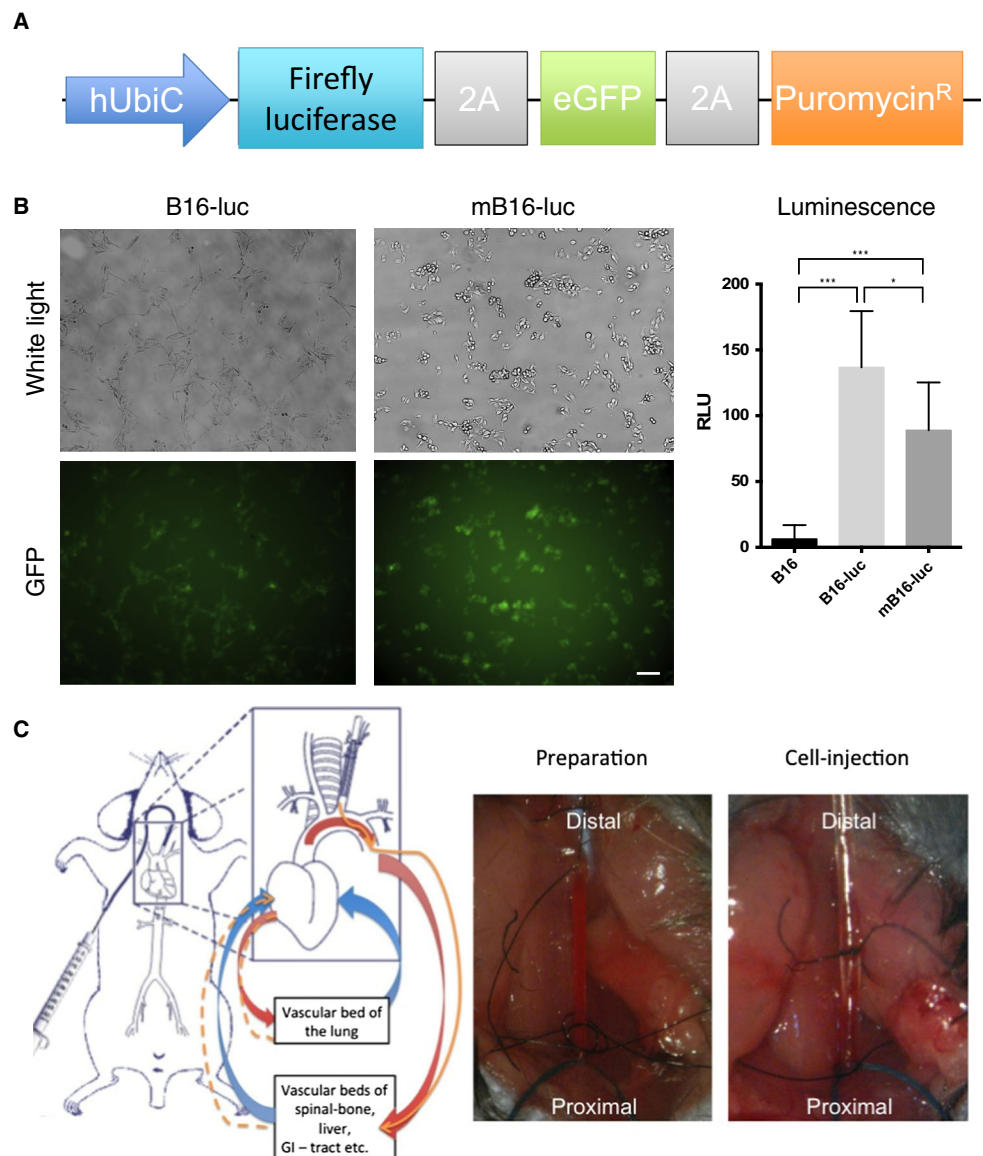
In vitro luminescence of different cell numbers lysates generated a standard curve defining relative light units (RLU) for individual cell numbers. Standard curve was generated as follows: cells were counted with Casy Model TT (Roche, Basel, CH) cell counter and were diluted to 100,000, 50,000, 25,000, 12,500, 6250, 3125 and 1562.5 per 96 well. Cells were lysed with 30 µl luciferase lysis buffer, 60 µl of Bright-Glo luciferase substrate was added and luminescence signal was measured (Promega,

Fig. 1 Vector design, injection protocol and MRI analysis.

a The vector was designed to contain T2A self-cleaving peptide sequences. The firefly luciferase gene was cloned using HindIII/AflII restriction sites, eGFP was inserted using KpnI/AvrII sites and puromycin resistance was inserted with SpeI/NotI restriction sites.

b B16-luc and mB16-luc cells did not show significant differences in morphology. GFP expression was found in both cell types (*scale bar 500 μm*). B16-luc and mB16-luc luminescence was increased compared to uninfected B16-F1 cells (One way anova, Dunnett post hoc analysis, $n = 5$, graph shows mean \pm SD).

c Schematic drawing shows hypothetical cell dissemination after retrograde carotid artery injection (*red* arterial vessels, *blue* venous vessels, *orange line straight* direct cell flow and *orange line dotted* possible further cell flow). Operation window shows preparation a priori of catheter insertion (*left*) and after catheter insertion and during cell injection (*right*)



Madison, WI, USA). Tissue homogenate (30 μl) was used to analyze metastatic growth in different organs.

Retrograde carotid artery injection

Animal experiments were performed according to local animal welfare guidelines. PCR protocols of intercellular adhesion molecule-1 knockout (*ICAM-1^{-/-}*, Jax # 002127) animals were described previously. Adult mice were anesthetized and anesthesia was verified by foot paw pinching reflex control. A catheter (0.8 mm Ø and 5 cm length) was placed on a 30 G injection needle and filled with 0.9 % NaCl solution. A longitude skin incision along the trachea was performed. The parotid gland was divided to expose the left carotid artery. The carotid artery was carefully separated from the vagus nerve and permanently/

temporarily ligated distally and proximally of the aortic arch, respectively. The artery was opened and the catheter was retrogradely inserted and fixed (Fig. 1b). The proximal ligature was opened and 100 μl of DMEM/cell suspension or DMEM/microbeads suspension was injected followed by 100 μl 0.9 % NaCl. The proximal ligature was closed permanently and the catheter was removed. The skin was closed and sutured.

Metastasis screening using bioluminescence analysis in vivo

Bioluminescence imaging was performed using the IVIS Lumina II (Caliper LS, Hopkinton, MA, USA) equipment. The mice were anesthetized using 2 % isoflurane. D-luciferine (Caliper LS) solution (30 mg/ml) was injected as

described in the manufacturers' protocol (10 $\mu\text{l/g}$ BW). In vivo luminescence was measured for 5 min dorsally and 5 min ventrally. Mice were shaved dorsally along the spinal tract for dorsal imaging.

Magnetic resonance imaging

Occurrence of a neurological deficit and/or suggestion of spinal metastasis by bioluminescence imaging was followed by spinal MRI to verify or exclude spinal metastasis formation. MRI was performed using a 7 Tesla rodent scanner (Pharmascan 70/16AS, Brucker, Billerica, MA, USA) with a 16 cm horizontal bore magnet and a 1H-RF-Volume resonator (72 mm) for transmission (Rapid Biomed, Rimpur, DE, USA) were used. The H-resonance frequency was 300 MHz, maximum gradient strength was 300mT/m. Paravision 5.1 (Brucker) was used to acquire images. Mice were anesthetized using 2 % isoflurane in O₂/NO₂ (30/70 %). Anesthetized mice were placed dorsally on top of a 37 °C heating pad with the incisions fixed and constant anesthesia supplied. Ventilation was monitored throughout the scan. A T2-weighted 2D turbo spin-echo sequence was used to visualize the spine. 10 sagittal slices (0.5 × 30 × 30 mm) were positioned over the spine. Data was analyzed with Amira software. Spinal metastases were identified using false coloring (Fig. 1c). Number of vertebral segments affected, mean metastasis and total metastasis volume were analyzed.

Tissue homogenization

Animals were sacrificed at the occurrence of neurological symptoms. Multi-organ resection was performed. Organs were frozen in Isopentane. Using mortar and pestle, tissues were homogenized to fine powder at –80 °C cooling with liquid nitrogen. Powder and soft tissue organs were transferred to individual gentleMACS tubes. Luciferase lysis buffer (0.1 M Tris-HCl, 0.1 % Triton X-100, 2 mM EDTA) was added to soft tissues and to grinded hard tissues. Dispomix (Miltenyi Biotec, Bergisch Gladbach, DE) profile 4 (4000 rpm for 15 s) was performed four times. MACS tubes were centrifuged for 5 min at 1200g/4 °C. Supernatant was decanted for the assay. Luciferase assay was performed as described previously [13].

Statistical analysis

Quantitative data are given as mean \pm SD. Mean values of all parameters were calculated from the average values in each animal. For analysis of differences, ANOVA followed by Bonferroni correction was used. For comparisons between groups, Student's *t* test was performed. Results with $p < 0.05$ were considered significant. Prism 6 (Graphpad,

La Jolla, CA, USA) software was used for statistical analysis.

Results

Luciferase activity in tumor cell lines

B16-luc cells demonstrated significantly increased luminescence activity after luciferin stimulation as compared to control cells (Control: 6.4 ± 10.53 , B16-luc: 136.7 ± 42.73). After in vivo application and isolation from a metastatic site, mB16-luc cells demonstrated stable luminescence activity as compared to B16-luc and significantly increased luminescence activity as compared to controls (mB16-luc: 89 ± 36.27 , Fig. 1b).

Long-term spinal metastasis formation

Using B16-luc cells spinal metastasis developed over an observation period of 26.5 days (Fig. 2). In vivo selected mB16-luc cells induced a neurological phenotype significantly earlier (21 days, $p = 0.0067$, Fig. 2c). In mB16-luc, number of spinal metastasis (B16-luc: 1.2 ± 0.447 , mB16-luc: 3.2 ± 1.643) and total spinal metastasis volume (B16-luc: $2.87 \pm 2.453 \text{ mm}^3$, mB16-luc: $11.19 \pm 3.898 \text{ mm}^3$) was significantly increased compared to B16-luc (Fig. 2d, e). No difference between both groups was observed in mean spinal metastasis volume (Fig. 2f).

Spinal metastasis under ICAM1 depletion

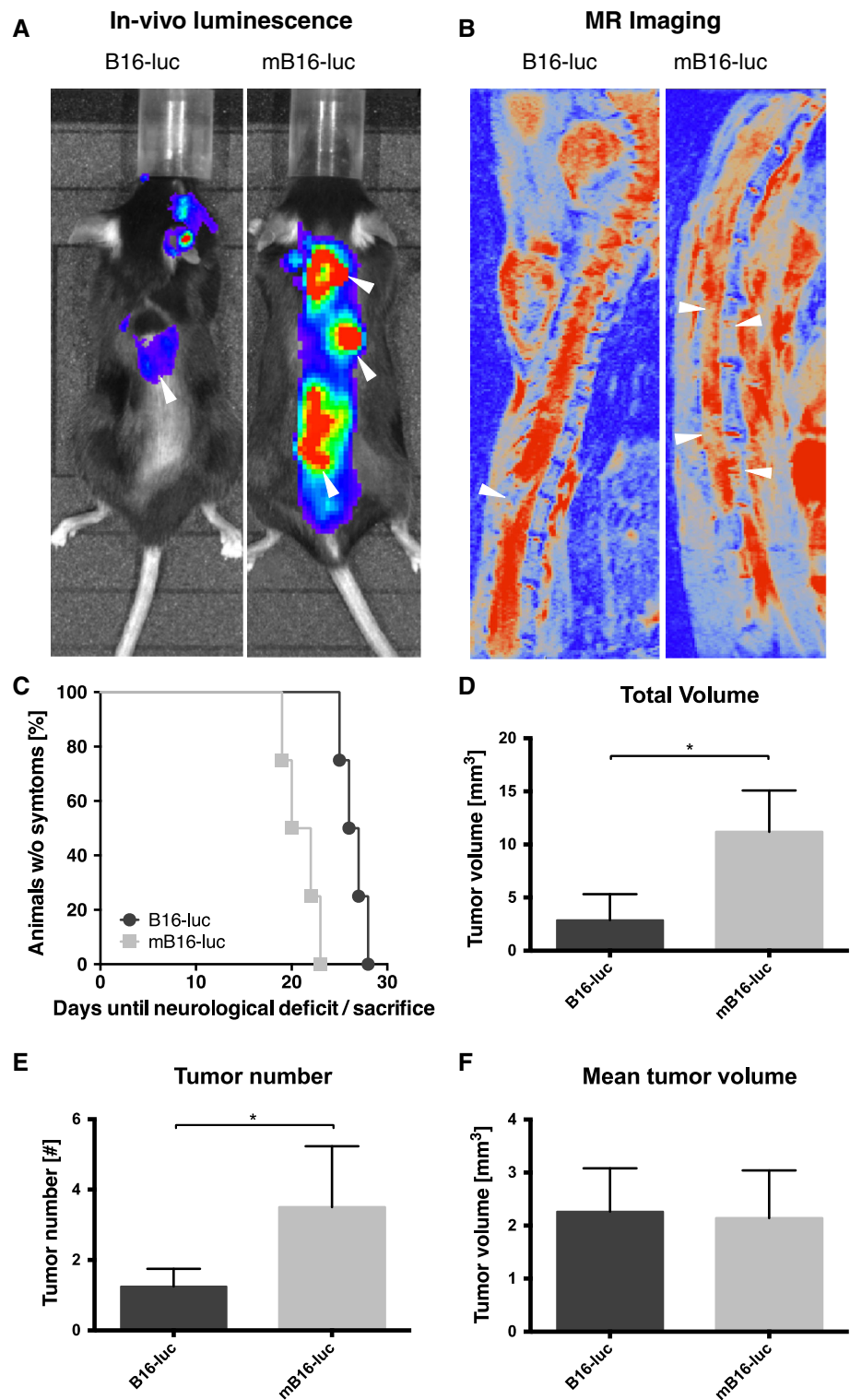
In *ICAM-1*^{-/-} animals a neurological phenotype developed significantly later as in mB16-luc (*ICAM-1*^{-/-} = 29 days; mB16-luc = 19.5 days, $p = 0.0133$, Fig. 3a–c). MRI analysis revealed significant reduction of total spinal metastasis volume (control: $10.03 \pm 4.25 \text{ mm}^3$; *ICAM-1*^{-/-}: $1.53 \pm 0.81 \text{ mm}^3$; $p < 0.05$), number (control: = 3.75 ± 1.90 ; *ICAM-1*^{-/-} = 1.20 ± 0.84 , $p < 0.05$) and mean metastasis volume (control: $2.41 \pm 1.37 \text{ mm}^3$; *ICAM-1*^{-/-}: $1.02 \pm 0.54 \text{ mm}^3$, $p < 0.05$).

Organ-specific metastasis distribution

To analyze organ-specificity of this metastatic process, we used luminescence analysis. The slope of the fluorescence standard curve was 17.58 with 16.20–18.87 95 % confidence interval ($R^2 = 0.9711$). Organ-specific metastasis distribution demonstrated long-term metastasis growth in osseous organs using mB16-luc in control animals (cranium: $2.004 \times 10^7 \pm 1.501 \times 10^7$ cells/organ, long-bones: $1.372 \times 10^7 \pm 1.511 \times 10^7$ cells/organ, spine: $3.261 \times 10^6 \pm 5.426 \times 10^6$ cells/organ). Soft tissue

Fig. 2 Evaluation of spinal metastasis formation using B16-luc and mB16-luc.

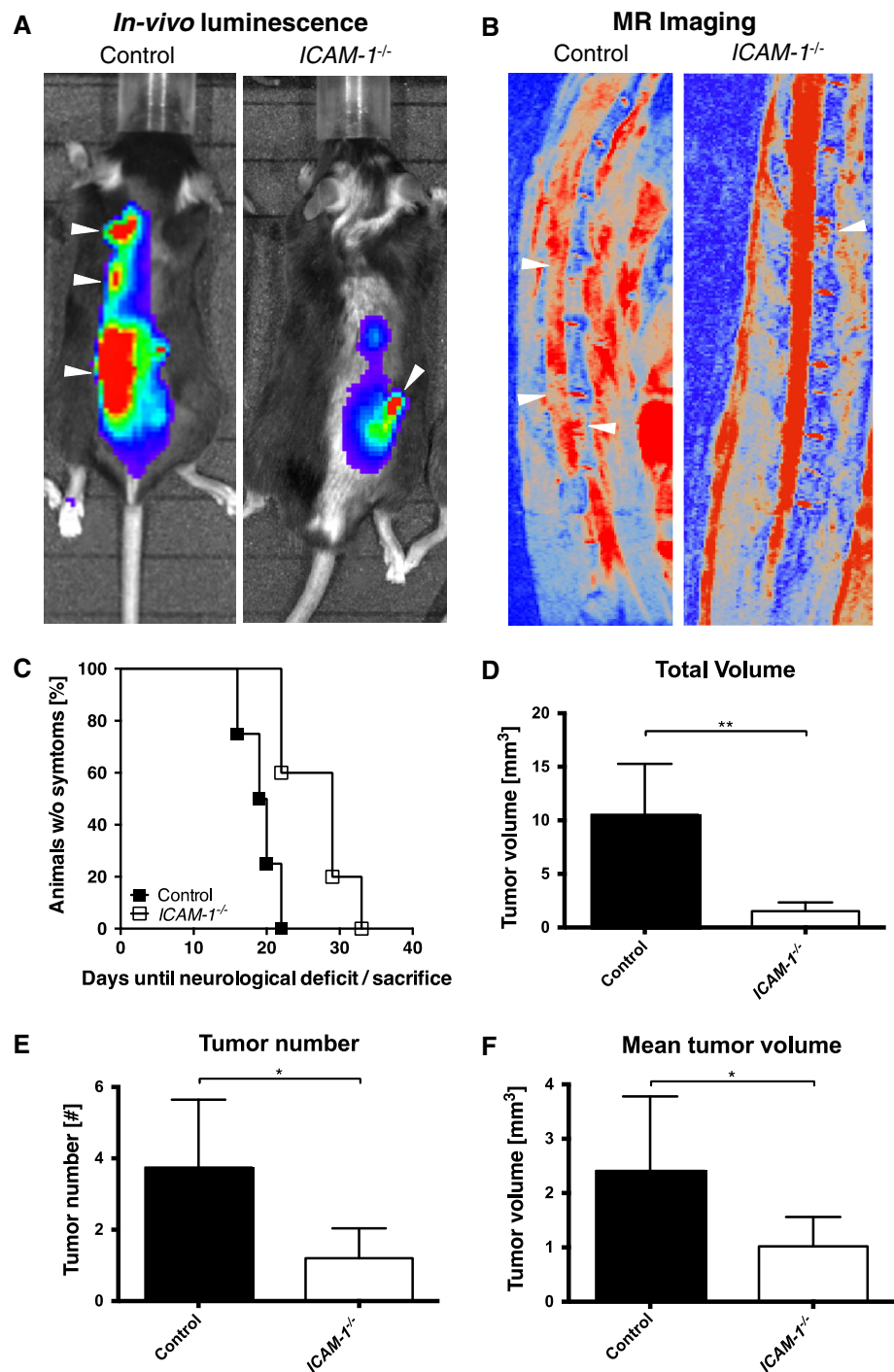
a Bioluminescence analysis indicated increased metastasis formation in mB16-luc—**injected animals.** **b** MR imaging (*false color* coded) demonstrates increased number of metastatic loci in mB16-luc (*white arrowheads*). **c** Graph demonstrates Kaplan–Meier survival plot for neurological function (T Log-rank, Mantel–Cox test; $p = 0.0186$). Graphs quantifying total spinal metastasis volume (**d**), number of spinal metastasis (**e**) and mean volume of individual spinal metastasis (**f**)



organs demonstrated a very low metastatic tumor cell load without metastatic cells in the brain (Fig. 4a). Consequently, a significant bone preference is demonstrated in mB16-luc animals (bone = $2.30 \times 10^7 \pm 6.54 \times 10^6$; other = $4.35 \times 10^6 \pm 4.62 \times 10^6$; Fig. 4a).

Analysis of long-term metastasis development in *ICAM-1*^{-/-} animals showed a generally decreased metastasis load with significantly reduced metastatic cell numbers in: spine (1353 ± 903 cells/organ), long-bones (9797 ± 7797 cells/organ), heart (3283 ± 6186 cells/organ), liver

Fig. 3 ICAM1 knockout animals show delayed paraplegia and less spinal tumor volume. **a** In vivo bioluminescence imaging 15 days post tumor cell injection shows reduced tumor load in ICAM1 knockout animals (white arrows). $N \leq 4$. **b** False color MRI at day of phenotype/sacrifice shows multiple compressive loci and affected vertebral bodies in controls. *ICAM-1*^{-/-} animals demonstrate reduced tumor loci (white arrow) and reduced spinal compression. **c** Kaplan–Meier survival plot for neurological function demonstrates a significantly prolonged time period until a neurological phenotype due to spinal cord compression develops in *ICAM-1*^{-/-} animals (Log-rank Mantel–Cox test $p = 0.0133$, Gehan–Breslow–Wilcoxon test $p = 0.0143$; $N = 4$). *ICAM-1*^{-/-} depletion leads to a reduction of total volume (**d**), number (**e**) and mean volume (**f**) of spinal metastasis (Two tailed unpaired t test, $n = 4$, $p = 0.0093$, graph shows mean \pm SD)

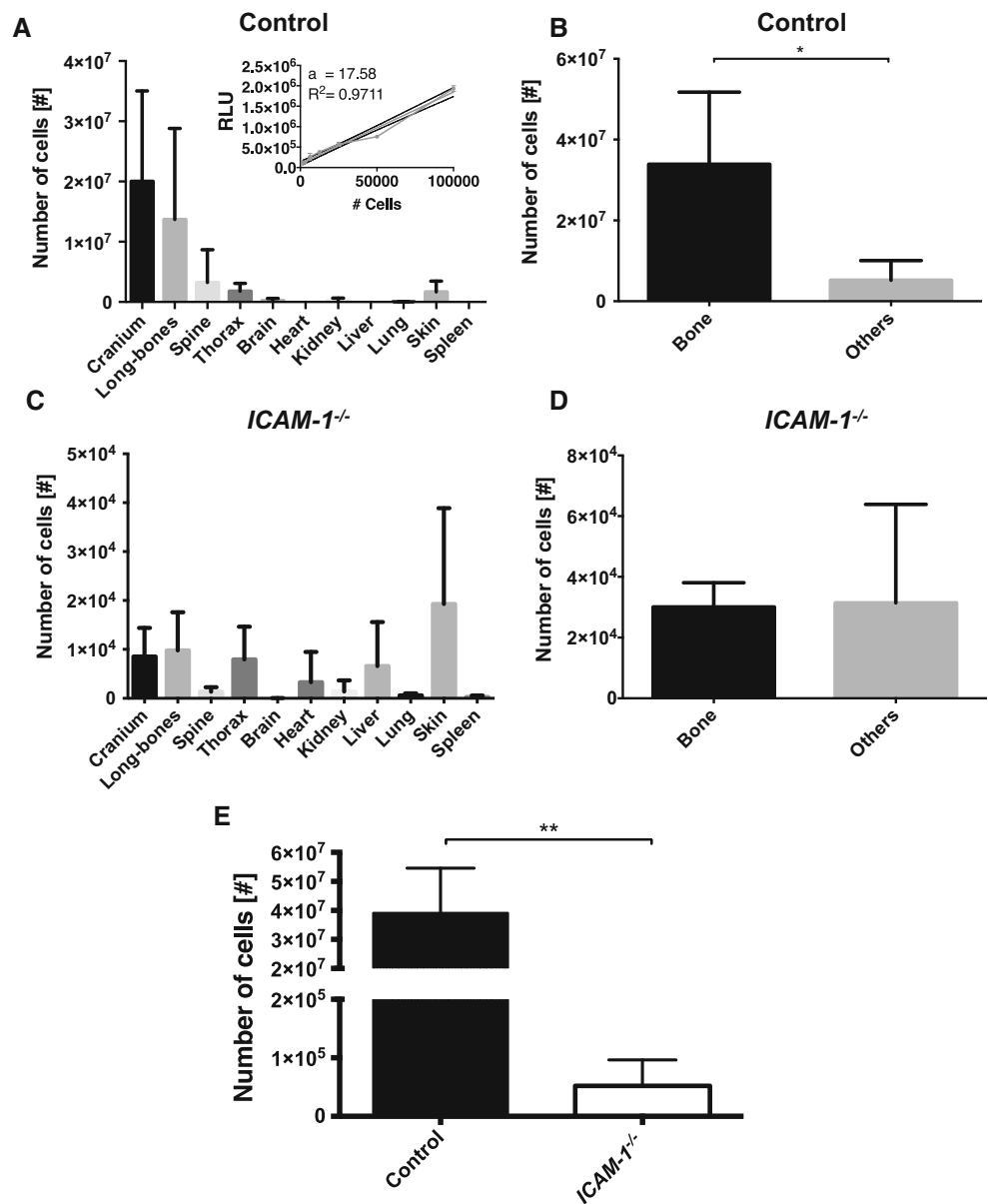


(6951 \pm 9008 cells/organ), lung (584 \pm 405 cells/organ) and spleen (287 \pm 276 cells/organ; Fig. 4). Total metastatic load in all organs was reduced 700-fold in *ICAM-1*^{-/-} animals as compared to mB16-luc (mB16-luc = $3.47 \times 10^7 \pm 1.66 \times 10^7$; *ICAM-1*^{-/-} = $5.20 \times 10^4 \pm 4.44 \times 10^4$; Fig. 4e).

Discussion

In this study we demonstrated reliable spinal metastasis generation and imaging in mice using intraarterial injection of B16-luc cells. Generation of in vivo selected mB16-luc cells increased number and volume of spinal metastasis and

Fig. 4 Organ-specific distribution of metastasis in control and *ICAM-1^{-/-}* animals. **a, b** Fluorescence analysis demonstrates significantly increased metastasis development in osseous organs (e.g., cranium, long bones and spine) compared to soft tissue organs in control animals (Student's *t* test, two tailed, unpaired, $n = 4$, $p = 0.021$, graph shows mean \pm SD). **c, d** Metastasis quantification demonstrates reduced metastatic burden in *ICAM-1^{-/-}* animals without a bone preference (Student's *t* test, two tailed, unpaired, $n = 4$, $p = 0.021$, graph shows mean \pm SD). **e** Quantification of general metastatic tumor cell burden demonstrates significantly reduced number of metastasis in *ICAM-1^{-/-}* animals (Student's *t* test, two tailed, $n = 4$, $p = 0.0045$, graph shows mean \pm SD)



lead to an earlier manifestation of neurological deficits. Under ICAM1 depletion, spinal metastasis was significantly reduced with a significant delay in the time until a neurological deficit occurrence. Hence, ICAM1 depletion provoked organ-unspecific reduction of metastasis development. Intraarterial injection of B16 melanoma cells reliably allows the generation of spinal metastasis. Application of these cells leads to spinal metastasis at an early time point (15–25 days after injection), before the non-osseous metastasis load limits the general status of experimental animals. Therefore, these cells represent ideal tumor cells to specifically investigate mechanisms of spinal metastasis. Arguello et al. [14] demonstrated that injection of 100.000 melanoma cells leads to metastasis formation in

the spine after intracardiac injection. However, intracardiac injection of B16 melanoma cells results in brain metastasis in 30 % of mice [14]. To exclude interference of neurological phenotypes resulting from brain and spinal metastasis, we modulated the experimental approach and performed retrograde injection of tumor cells into the left carotid artery. This approach circumvents intracranial circulation by applying tumor cells into the distal aortic arch, so that tumor cells primarily distribute in the remaining organ circulation. Sacrifice of the left carotid artery does not induce a risk for cerebral ischemia, as collateralization routes compensate for the non-perfused left carotid artery after occlusion in mice [1, 15]. Consequently, we did not identify metastases in the brain. Therefore, neurological

symptoms could only be explained by myelon compression due to spinal metastasis reflecting human spinal metastatic disease in our experiments.

To increase metastatic potential of B16-luc cells to the spine, we isolated tumor cells from spinal metastasis and performed reinjection of these *in vivo* selected, metastatic tumor cells, increasing spinal metastasis and reducing the time until a neurological deficit develops. Organ-specific metastasis distribution analysis showed that increased spinal metastasis in mB16-luc is not a spine-specific phenomenon, but the result of preferential metastasis development in osseous organs in general. In support of this observation, Stackpole et al. [16] demonstrated an organ-unspecific increase in secondary metastatic activity regardless of the primary metastatic site or the number of injection cycles using B16 melanoma cells in *in vivo* selection experiments. Under ICAM1 depletion spinal metastatic disease was significantly reduced leading to a significant delay in the time until a neurological deficit developed. In support of this data are several clinical and experimental studies that show that high ICAM1 activity is associated with tumor or metastasis progression whereas ICAM1 depletion leads to reduced metastasis formation [6–8, 17, 18]. In bone metastasis, ICAM1 also plays an important role in mediating metastasis development [6]. ICAM1 has been shown to mediate tumor cell–endothelial cell interactions inducing recruitment of neutrophils that stimulate the release of chemokines and cytokines [19]. These molecules induce breakdown of endovascular barriers and thereby promote metastasis formation [19]. In bone metastasis, ICAM1 expression has been linked to the expression of the chemokine CCL2, which negatively regulates bone metastasis formation in a breast cancer model [20]. However, it remains unclear if the observations of our study are the result of increased extravasation of tumor cells into bone tissue or if they are the result of mechanisms that occur after tumor cells have entered the target organ.

Our data demonstrate that metastasis formation is decreased in every organ under ICAM1 depletion indicating that ICAM1 depletion leads to a generally reduced metastasis development without bone specific or spine-specific effects. In humans, breast cancer micrometastasis has been shown to be characterized by increased expression of ICAM1 [21]. A recent report further demonstrated that ICAM1 is involved in regulating osteoclast miRNA changes in human osteolytic bone metastasis [22]. In malignant lymphoma, antimetastatic effects have been described to occur after cells have extravasated into the target organ [7]. However, the exact molecular mechanism how ICAM1 influences spinal bone metastasis remains unknown. ICAM1 depletion may act antimetastatic in osseous organs by affecting bone metabolism and osteoclast-tumor

cell interactions (post-homing effects) or it may affect metastatic tumor cell homing to the spinal bone by altering tumor–cell endothelial cell interactions [23, 24].

In conclusion we present a reliable experimental spinal metastasis model in mice that allows morphological and clinical spinal metastasis analysis. Applying this model we demonstrate that *in vivo* selected tumor cells show both a bone and spine preference in their metastatic behavior resulting in aggravated spinal metastatic disease. ICAM1 depletion reduces metastasis formation in the spine as result of an organ-unspecific antimetastatic effect.

Acknowledgments T.B. is a doctoral student of the Ph.D Program Medical Neuroscience Charité and received the Ernst von Leyden stipend of the Berliner Krebsgesellschaft e.V. M.C. was part of the Friedrich C. Luft Clinical Scientist Pilot Program funded by the Volkswagen Foundation and the Charité Foundation.

Conflict of interest None.

References

1. Kitagawa K, Yagita Y, Sasaki T, Sugiura S, Omura-Matsuoka E, Mabuchi T, Matsushita K, Hori M (2005) Chronic mild reduction of cerebral perfusion pressure induces ischemic tolerance in focal cerebral ischemia. *Stroke J Cereb Circ* 36:2270–2274. doi:10.1161/01.STR.0000181075.77897.0e
2. Klimo P Jr, Schmidt MH (2004) Surg Manage Spinal Metastases. *Oncologist* 9:188–196
3. Ryken TC, Eichholz KM, Gerszten PC, Welch WC, Gokaslan ZL, Resnick DK (2003) Evidence-based review of the surgical management of vertebral column metastatic disease. *Neurosurg Focus* 15:E11
4. Patchell RA, Tibbs PA, Regine WF, Payne R, Saris S, Kryscio RJ, Mohiuddin M, Young B (2005) Direct decompressive surgical resection in the treatment of spinal cord compression caused by metastatic cancer: a randomised trial. *Lancet* 366:643–648. doi:10.1016/S01406736(05)669541
5. Gay LJ, Felding-Habermann B (2011) Contribution of platelets to tumour metastasis. *Nat Rev Cancer* 11:123–134. doi:10.1038/nrc3004
6. Takahashi M, Furihata M, Akimitsu N, Watanabe M, Kaul S, Yumoto N, Okada T (2008) A highly bone marrow metastatic murine breast cancer model established through *in vivo* selection exhibits enhanced anchorage-independent growth and cell migration mediated by ICAM-1. *Clin Exp Metastasis* 25:517–529. doi:10.1007/s1058500891635
7. Aoudjit F, Potworowski EF, Springer TA, St-Pierre Y (1998) Protection from lymphoma cell metastasis in ICAM-1 mutant mice: a posthoming event. *J Immunol* 161:2333–2338
8. Hayes SH, Seigel GM (2009) Immunoreactivity of ICAM-1 in human tumors, metastases and normal tissues. *Int J Clin Exp Pathol* 2:553–560
9. Rosette C, Roth RB, Oeth P, Braun A, Kammerer S, Ekblom J, Denissenko MF (2005) Role of ICAM1 in invasion of human breast cancer cells. *Carcinogenesis* 26:943–950. doi:10.1093/carcin/bgi070
10. Datwyler AL, Lattig-Tunnemann G, Yang W, Paschen W, Lee SL, Dirnagl U, Endres M, Harms C (2011) SUMO2/3 conjugation is an endogenous neuroprotective mechanism. *J Cereb Blood Flow Metab Off J Int Soc Cereb Blood Flow Metab* 31:2152–2159. doi:10.1038/jcbfm.2011.112

11. Lois C, Hong EJ, Pease S, Brown EJ, Baltimore D (2002) Germline transmission and tissue-specific expression of transgenes delivered by lentiviral vectors. *Science* 295:868–872. doi:[10.1126/science.1067081](https://doi.org/10.1126/science.1067081)
12. Dittgen T, Nimmerjahn A, Komai S, Licznarski P, Waters J, Margrie TW, Helmchen F, Denk W, Brecht M, Osten P (2004) Lentivirus-based genetic manipulations of cortical neurons and their optical and electrophysiological monitoring in vivo. *Proc Natl Acad Sci USA* 101:18206–18211. doi:[10.1073/pnas.0407976101](https://doi.org/10.1073/pnas.0407976101)
13. Heroult M, Schaffner F, Pfaff D, Prahst C, Kirmse R, Kutschera S, Riedel M, Ludwig T, Vajkoczy P, Graeser R, Augustin HG (2010) EphB4 promotes site-specific metastatic tumor cell dissemination by interacting with endothelial cell-expressed ephrinB2. *Mol Cancer Res MCR* 8:1297–1309. doi:[10.1158/15417786.MCR090453](https://doi.org/10.1158/15417786.MCR090453)
14. Arguello F, Baggs RB, Frantz CN (1988) A murine model of experimental metastasis to bone and bone marrow. *Cancer Res* 48:6876–6881
15. Hecht N, He J, Kremenetskaia I, Nieminen M, Vajkoczy P, Woitzik J (2012) Cerebral hemodynamic reserve and vascular remodeling in C57/BL6 mice are influenced by age. *Stroke. a journal of cerebral circulation* 43:3052–3062. doi:[10.1161/STROKEAHA.112.653204](https://doi.org/10.1161/STROKEAHA.112.653204)
16. Stackpole CW, Alterman AL, Valle EF (1991) B16 melanoma variants selected by one or more cycles of spontaneous metastasis to the same organ fail to exhibit organ specificity. *Clin Exp Metastasis* 9:319–332
17. Natali P, Nicotra MR, Cavaliere R, Bigotti A, Romano G, Temponi M, Ferrone S (1990) Differential expression of intercellular adhesion molecule 1 in primary and metastatic melanoma lesions. *Cancer Res* 50:1271–1278
18. Lalancette M, Aoudjit F, Potworowski EF, St-Pierre Y (2000) Resistance of ICAM-1-deficient mice to metastasis overcome by increased aggressiveness of lymphoma cells. *Blood* 95:314–319
19. Roland CL, Harken AH, Sarr MG, Barnett CC Jr (2007) ICAM-1 expression determines malignant potential of cancer. *Surgery* 141:705–707. doi:[10.1016/j.surg.2007.01.016](https://doi.org/10.1016/j.surg.2007.01.016)
20. Takahashi M, Miyazaki H, Furihata M, Sakai H, Konakahara T, Watanabe M, Okada T (2009) Chemokine CCL2/MCP-1 negatively regulates metastasis in a highly bone marrow-metastatic mouse breast cancer model. *Clin Exp Metastasis* 26:817–828. doi:[10.1007/s1058500992818](https://doi.org/10.1007/s1058500992818)
21. Aherne NJ, ETC, Wang JH, Redmond KC, Kelly J, Richardson D, Redmond HP (2002) Bone marrow micrometastases have upregulation of ICAM-1 and $\alpha V\beta 3$ integrins: a putative survival mechanism for tumour dissemination? *Irish J Med Sci* 171:2. doi:[10.1007/BF03170404](https://doi.org/10.1007/BF03170404)
22. Ell B, Mercatali L, Ibrahim T, Campbell N, Schwarzenbach H, Pantel K, Amadori D, Kang Y (2013) Tumor-induced osteoclast miRNA changes as regulators and biomarkers of osteolytic bone metastasis. *Cancer Cell* 24:542–556. doi:[10.1016/j.ccr.2013.09.008](https://doi.org/10.1016/j.ccr.2013.09.008)
23. Lavigne P, Benderdour M, Shi Q, Lajeunesse D, Fernandes JC (2005) Involvement of ICAM-1 in bone metabolism: a potential target in the treatment of bone diseases? *Expert Opin Biol Ther* 5:313–320. doi:[10.1517/14712598.5.3.313](https://doi.org/10.1517/14712598.5.3.313)
24. Zhang P, Goodrich C, Fu C, Dong C (2014) Melanoma upregulates ICAM-1 expression on endothelial cells through engagement of tumor CD44 with endothelial E-selectin and activation of a PKC α -p38-SP-1 pathway. *FASEB J Off Publ Fed Am Soc Exp Biol* 28:4591–4609. doi:[10.1096/fj.11202747](https://doi.org/10.1096/fj.11202747)